



Resolving the Emission Regions of the Crab Pulsar’s Giant Pulses

Robert Main^{1,2,3} , Rebecca Lin², Marten H. van Kerkwijk² , Ue-Li Pen^{3,4,5,6} , Alexei G. Rudnitskii⁷ , Mikhail V. Popov⁷, Vladimir A. Soglasnov⁷, and Maxim Lyutikov⁸ 

¹ Max-Planck-Institut für Radioastronomie, Auf dem Hügel 69, D-53121, Bonn, Germany

² Department of Astronomy and Astrophysics, University of Toronto, 50 St. George Street, Toronto, ON M5S 3H4, Canada

³ Canadian Institute for Theoretical Astrophysics, University of Toronto, 60 St. George Street, Toronto, ON M5S 3H8, Canada

⁴ Dunlap Institute for Astronomy and Astrophysics, University of Toronto, 50 St. George Street, Toronto, ON M5S 3H4, Canada

⁵ Canadian Institute for Advanced Research, 180 Dundas Street West, Toronto, ON M5G 1Z8, Canada

⁶ Perimeter Institute for Theoretical Physics, 31 Caroline Street North, Waterloo, ON N2L 2Y5, Canada

⁷ Astro Space Center, Lebedev Physical Institute, Russian Academy of Sciences, Profsoyuznaya ul. 84/32, Moscow, 117997 Russia

⁸ Department of Physics, Purdue University, 525 Northwestern Avenue, West Lafayette, IN 47907-2036, USA

Received 2020 April 30; revised 2021 May 14; accepted 2021 May 14; published 2021 July 7

Abstract

The Crab pulsar has striking radio emission properties, with the two dominant pulse components—the main pulse and the interpulse—consisting entirely of giant pulses. The emission is scattered in both the Crab Nebula and the interstellar medium, causing multipath propagation and thus scintillation. We study the scintillation of the Crab’s giant pulses using phased Westerbork Synthesis Radio Telescope data at 1668 MHz. We find that giant pulse spectra correlate at only $\sim 2\%$, much lower than the one-third correlation expected from a randomized signal imparted with the same impulse response function. In addition, we find that the main pulse and the interpulse appear to scintillate differently; the 2D cross-correlation of scintillation between the interpulse and main pulse has a lower amplitude and is wider in time and frequency delay than the 2D autocorrelation of the main pulses. These lines of evidence suggest that the giant pulse emission regions are extended, and that the main pulse and interpulse arise in physically distinct regions that are resolved by the scattering screen. Assuming the scattering takes place in the nebular filaments, the emission regions are of order a light-cylinder radius, as projected on the sky. With further very long baseline interferometry and multifrequency data, it may be possible to measure the distance to the scattering screens, the size of giant pulse emission regions, and the physical separation between the pulse components.

Unified Astronomy Thesaurus concepts: [Radio pulsars \(1353\)](#); [Interstellar scintillation \(855\)](#)

1. The Unusual Properties of the Crab Pulsar

The Crab pulsar is one of the most unusual radio pulsars and has been the subject of much observational and theoretical research (for a review, see Eilek & Hankins 2016). The two dominant components to its radio pulse profile, the main pulse and the low-frequency interpulse (simply referred to as the interpulse for the remainder of this paper), appear to be comprised entirely of randomly occurring giant pulses—extremely short and bright pulses of radio emission showing structure down to ns timescales and reaching intensities over a MJy (Hankins & Eilek 2007). Only the fainter components of the pulse profile—such as the precursor (to the main pulse)—are similar to what is seen for regular radio pulsars.

The main pulse and interpulse are aligned within 2 ms with emission components at higher energy, from optical to γ -ray (Moffett & Hankins 1996; Abdo et al. 2010), and giant pulses are associated with enhanced optical (Shearer et al. 2003; Strader et al. 2013) and X-ray (Enoto et al. 2021) emission. Because pair production strongly absorbs γ -ray photons inside the magnetosphere, this suggests that all these components arise far from the neutron star surface, with possible emission regions being the various magnetospheric “gaps” (Romani & Yadigaroglu 1995; Istomin 2004; Muslimov & Harding 2004; Qiao et al. 2004), induced Compton scattering in the upper magnetosphere (Petrova 2004, 2009), or regions outside the light cylinder (Philippov et al. 2019). In these regions, the giant pulses are thought to arise stochastically, likely triggered by plasma instabilities and/or reconnection (Eilek & Hankins 2016;

Philippov et al. 2019), from parts smaller, of order $\Gamma c\tau_{\text{pulse}} \simeq 0.1\dots 1$ km (with $\tau_{\text{pulse}} \sim 10$ ns the timescale of a pulse, and $\Gamma \sim 100$ an estimate of the relativistic motion), than the overall size of the emission region, of order $cP\delta\phi_{\text{pulse}} \sim 100$ km (with $\delta\phi_{\text{pulse}} \sim 0.01$ the width of the pulse phase window in which giant pulses occur).

While similar in their overall properties, the main pulse and interpulse have differences in detail. In particular, the interpulse has a large scatter in its dispersion measure compared to the main pulse, possibly suggesting that it is observed through a larger fraction of the magnetosphere (Eilek & Hankins 2016). In addition, it appears shifted in phase and shows “banding” in its power spectra above 4 GHz (the so-called “high-frequency interpulse”), with the spacing proportional to frequency (Hankins & Eilek 2007; Hankins et al. 2016).

The Crab pulsar, like many pulsars, exhibits scintillation from multipath propagation of its radio emission. The scattering appears to include both a relatively steady component, arising in the interstellar medium, and a highly variable one, originating in the Crab Nebula itself, with the former responsible for the angular and the latter for (most of) the temporal broadening (Rankin & Counselman 1973; Vandenberg 1976; Popov et al. 2017; Rudnitskii et al. 2017; McKee et al. 2018).

This scintillation offers the prospect of “interstellar interferometry,” where the high spatial resolution arising from multiple imaging is used to resolve the pulsar magnetosphere. This has been applied to some pulsars, with separations between emission regions inferred from time offsets (or phase gradients) between the scintillation patterns seen in different

pulse components. For some of these pulsars, the inferred separations were substantially larger than the neutron star radius: $\sim 10^3$ km for PSR B1237+25 (Wolszczan & Cordes 1987), $\gtrsim 100$ km for PSR B1133+16 (Gupta et al. 1999), and of order the light-cylinder radius (several 10^4 km) in a further four pulsars (Smirnova et al. 1996). In contrast, for PSR B0834+06, Pen et al. (2014) find only a very small positional shift, constraining the separation between emission regions to ~ 20 km, comparable to the neutron star radius.

In the above studies, the scintillation pattern offsets are small compared to the scintillation scale, i.e., the scintillation screen does not resolve the pulsar magnetosphere, but changes in position can be measured with data that have a high signal-to-noise ratio (S/N). For the Crab pulsar, however, the proximity of the nebular scattering screen to the pulsar implies that, as seen from the pulsar, the screen extends a much larger angle than would be the case if it were far away (for a given scattering time). Therefore the scintillation pattern is sensitive to small spatial scales, of order ~ 2000 km at our observing frequency (see Section 4.2), comparable to the light-cylinder radius $r_{LC} \equiv cP/2\pi \simeq 1600$ km.

The high spatial resolving power also implies that for a given relative velocity between the pulsar and the screen, the scintillation timescale is short. Indeed, from the scintillation properties of giant pulses, Cordes et al. (2004) infer a decorrelation time of ~ 25 s at 1.4 GHz. Unfortunately, their sample, while very large, had insufficient interpulse-main pulse pairs to look for differences between the two components (J. Cordes 2017, personal communication). From an even larger sample, Karuppusamy et al. (2010) identified pairs of pulses that either occurred in the same main-pulse phase window, or with one in the main pulse and one in the interpulse window. They did not find major differences between the sets. Like for the close pairs in Cordes et al. (2004), they found correlation coefficients consistent with the one-third expected for pulses that differ in their intrinsic time and frequency structure, but which have additional frequency structure imposed by scintillation.

In this paper, we compare the scintillation structure of the main pulse and the interpulse in more detail. We find that in our sample the frequency spectra of close pulses are much more weakly correlated than was seen previously, suggesting that during our observations, the scintillation pattern is sensitive to smaller spatial scales at the source than the separation between bursts (in effect, the scattering screen resolved the emission region). The scintillation patterns of the main pulse and interpulse also appear to differ, which, if taken at face value, suggests that their emission locations are offset in projection by of order a light-cylinder radius.

2. Observations and Data Reduction

We analyze 6 hr of data from the phased Westerbork Synthesis Radio Telescope (WSRT), and 2.5 hr of simultaneous data from the 305 m William E. Gordon Telescope at the Arecibo observatory (AR) that were taken as part of a RadioAstron observing run on 2015 January 10–11 (Popov et al. 2017). The data cover the frequency range of 1652–1684 MHz and consist of both circular polarizations in two contiguous 16 MHz channels, recorded using standard 2 bit Mark 5B format (WSRT), and VDIF (AR). The use of a telescope with high spatial resolution is particularly beneficial in studies of the Crab pulsar as it helps to resolve out the Crab

Nebula, effectively reducing the system temperature from 830 Jy (for the integrated flux at 1.7 GHz) to 165 Jy and 275 Jy for WSRT and AR, respectively (Popov et al. 2017).

To search for giant pulses, we coherently dedispersed⁹ the data from the two channels to a common reference frequency. Each 1 s segment of data was bandpass calibrated by channelizing the timestream into 8192 frequency channels per subband, normalizing by the square root of the time-averaged power spectrum. This correction works sufficiently well everywhere but at the band edges. RFI spikes above 5σ are removed using a 128-channel median filter, and time-variability is normalized by the square root of the frequency-averaged power spectrum. The signal was converted into complex by removing negative frequency components of the analytic representation signal (via a Hilbert transform) and shifting the signal down in frequency by half the signal bandwidth. After forming power spectra, we replace the outer 1 MHz (1652–1653 MHz, 1683–1684 MHz) and central 0.5 MHz (1667.75–1668.25 MHz) with the mean intensity in that time segment.

We search for giant pulses in a rolling boxcar window of $8 \mu\text{s}$ in steps of 62.5 ns (one sample in the complex timestream), summing the power from both channels and both polarizations. We flagged peaks above 8σ in the WSRT data, corresponding to ~ 60 Jy, as giant pulses, finding 15,232 events, i.e., a rate of $\sim 0.7 \text{ s}^{-1}$. This detection threshold was chosen to ensure there were no spurious detections. We find 4633 pulses above 8σ in the overlapping 2.5 hr of AR data, and all pulses have a detectable, higher S/N counterpart in WSRT. We show a sample main pulse that was detected at both telescopes, as well as the main pulse and interpulse nearby in time in Figure 1.

One possible concern is the effects of saturation from 2 bit recording, as described in Jenet & Anderson (1998). The dispersion sweep in our frequency range of 1652–1684 MHz is 3.26 ms, $\sim 100,000$ samples. Thus, even the strongest giant pulse with a peak flux density of ~ 100 kJy and duration of $3 \mu\text{s}$ will be reduced in intensity by roughly a thousand times, increasing the system temperature dS/S by only 35% and 60% for AR and WSRT, respectively, with the recording systems far from saturation. The majority of our pulses are much fainter, near our detection threshold of ~ 60 Jy, where saturation effects will be negligible.

3. Scintillation Properties

With the phased WSRT array, our pulse detection rate is sufficiently high that it becomes possible to compute a traditional dynamic spectrum by summing intensities as a function of time. We do this first below, as it gives an immediate qualitative view of the scintillation. A more natural choice for pulses that occur randomly in time, however, is to parameterize variations as a function of Δt , the time separation between pulses (Cordes et al. 2004; Popov et al. 2017). Hence, we continue by constructing correlation functions of the spectra as functions of both time and frequency offset.

⁹ Using a dispersion measure of $56.7716 \text{ pc cm}^{-3}$ appropriate for our date (taken from <http://www.jb.man.ac.uk/~pulsar/crab.html>; Lyne et al. 1993). We read in overlapping blocks of data, removed edges corrupted by dedispersion, such that the dedispersed data were contiguous in time.

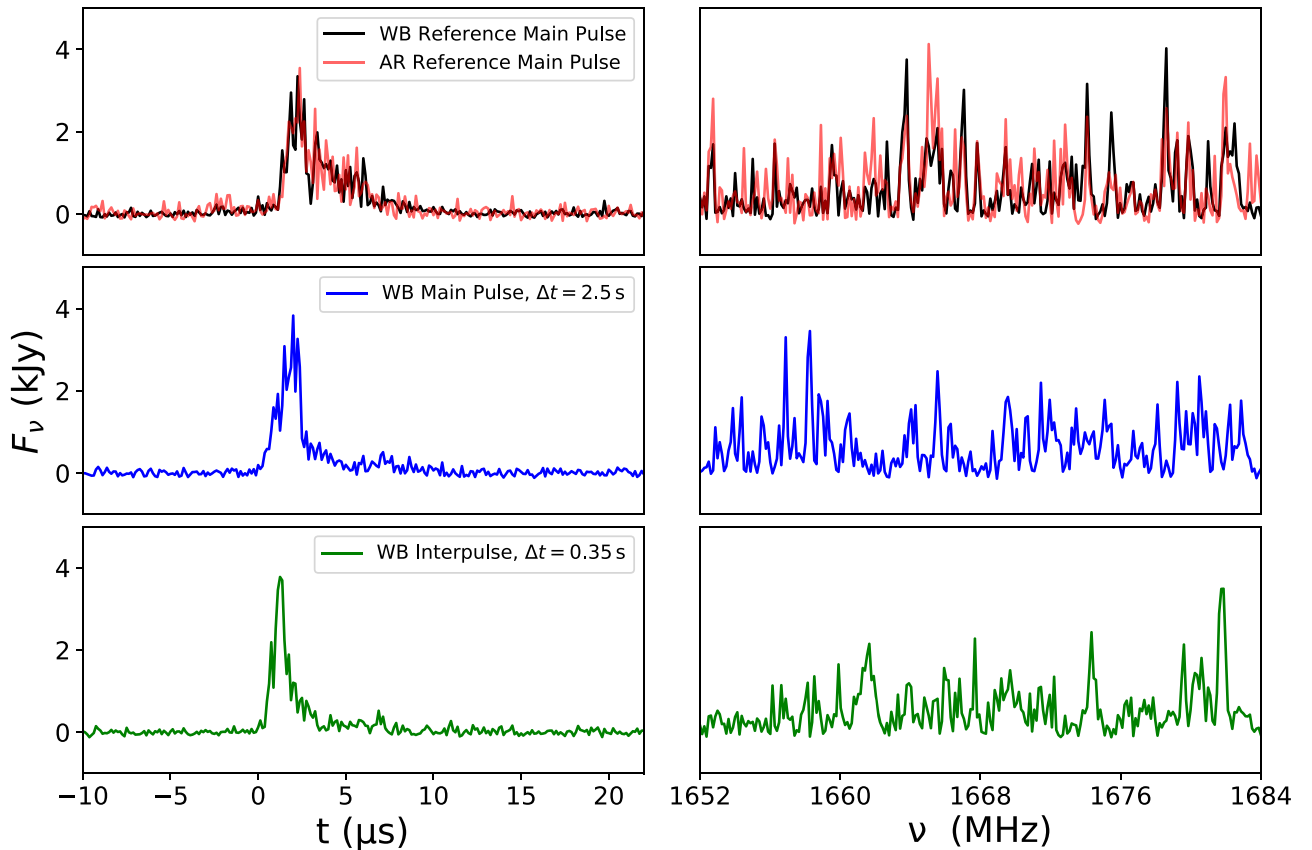


Figure 1. Top: Pulse profiles (left) and spectra (right) of a main pulse at both WSRT and AR. A nearby main pulse (middle) and interpulse (bottom) are shown for comparison, both separated by less than the scintillation timescale measured in Section 3.2. The profiles are shown in 125 ns bins, and the total flux is calculated using the T_{sys} values in Section 2. The spectra contain the emission from 0–8 μs in 125 kHz channels. The same pulse at WSRT and AR clearly shows a similar temporal and spectral structure, while the spectra of pulses within a scintillation time are drastically different, beyond what can be explained through the variable intrinsic structure in the pulse (discussed in detail in Section 4.1).

3.1. The Dynamic Spectrum of the Main Pulse

We construct the dynamic spectrum $I(t, \nu)$ by simply summing giant pulse spectra in each time bin. Because we wish to observe the scintillation pattern rather than the vast intrinsic intensity variations between giant pulses, we normalize each time bin by the total flux within that bin. While there will still be structure in the dynamic spectrum owing to the intrinsic time structure of the giant pulses (Cordes et al. 2004), any features in frequency that are correlated in time should only be associated with scintillation. We show a 20-minute segment of the dynamic spectrum in Figure 2. While noisy, the dynamic spectrum shows scintillation features. They are resolved by our time and frequency bin sizes of 4 s and 250 kHz, respectively, but only by a few bins, suggesting that the scintillation timescale and bandwidth are larger than our bin sizes by a factor of a few (consistent with $\nu_{\text{decorr}} = 1.10 \pm 0.02$ MHz, $t_{\text{scint}} = 9.2 \pm 0.13$ s measured below).

3.2. Correlation Functions

To infer the scintillation bandwidth and timescale, one usually uses the autocorrelation of the dynamic spectrum, but for pulses that are randomly spaced in time, it is easier to correlate spectra of pulse pairs and then bin by time separation Δt to create an estimate of the intrinsic correlation coefficient $\rho(\Delta\nu, \Delta t)$ (Cordes et al. 2004).

For two spectra $P_1(\nu)$ and $P_2(\nu)$, the expected correlation coefficient is given by

$$\rho_{12}(\Delta\nu) = \frac{\langle (P_1(\nu) - \mu_1)(P_2(\nu + \Delta\nu) - \mu_2) \rangle}{\sigma_1 \sigma_2}, \quad (1)$$

where $\Delta\nu$ is the offset in frequency, μ_1 , μ_2 , σ_1^2 and σ_2^2 are expectation values for the means and intrinsic variances of P_1 and P_2 , and we use $\langle \dots \rangle$ to indicate the expectation value of the product. If the giant pulses were effectively delta functions in our band, but affected by the same impulse response function associated with the scintillation, one would expect $\rho = 1$ for $\Delta\nu = 0$, and a fall-off in frequency and time difference with the appropriate scintillation bandwidth and timescale, approaching 0 at large $\Delta\nu$ and Δt_{12} . As noted by Cordes et al. (2004), however, if each pulse consists of multiple shots, the spectra of two pulses will have a different structure, and if they are still affected by the same impulse response function, one expects a reduced peak, with maximum $\rho \simeq 1/3$ (as was indeed observed in their data set).

From observed spectra, one can only estimate the correlation coefficient. As we show in the Appendix, if one simply uses the standard equation for the sample correlation coefficient, using the sample mean m and sample variance s^2 as estimates of μ and σ^2 , the result is biased in the presence of background noise,

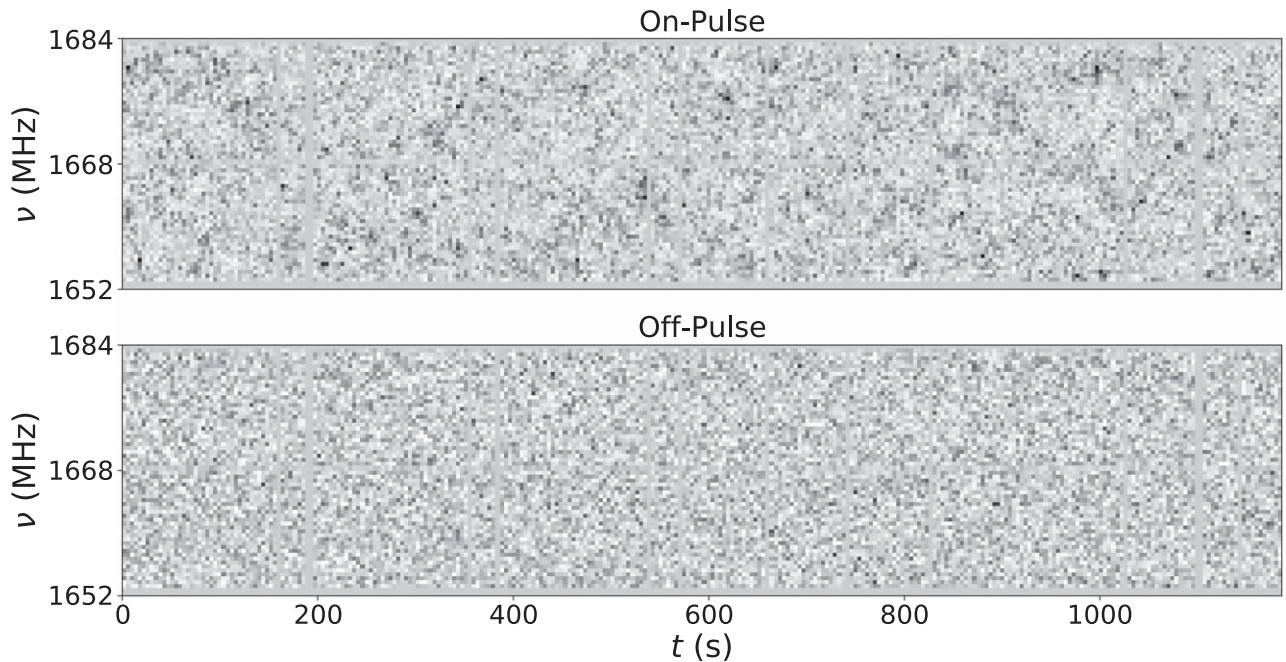


Figure 2. Top: Part of the dynamic spectrum inferred from the main pulse by summing individual giant pulse spectra at 250 kHz resolution in 4 s bins. The total flux in each time bin was normalized to remove the effects of variable pulse brightness. The random occurrence of giant pulses and their variable flux means that the noise properties of the time bins are heterogeneous and that some bins have no flux. Bottom: Dynamic spectrum of an off-pulse region before each giant pulse, processed in the same way as in the top panel. Artifacts from the bandpass are apparent at 1668 MHz, and at the band edges, which are masked in further analysis. The off-pulse region shows heterogeneous noise due to the variable number of “pulses” in each time bin, reflecting the uneven sampling of giant pulses. The color bars are saturated to $\mu_{\pm 2\sigma}^{\pm 2\sigma}$, where μ and σ are the mean and standard deviation of the on-pulse dynamic spectrum.

but an unbiased estimate can be made using

$$r_{12}(\Delta\nu) = \frac{1}{k-1} \sum_{i=1}^k \frac{(P_1(\nu_i) - m_1)(P_2(\nu_i + \Delta\nu) - m_2)}{s_1 s_2} \times \left(\frac{m_1 m_2}{(m_1 - m_b)(m_2 - m_b)} \right), \quad (2)$$

where m_b is the mean power in the background.

We create spectra for pulses using the $8 \mu\text{s}$ bin centered at each peak, yielding 125 kHz channels. To ensure sufficiently reliable correlations between pulse pairs, we limited ourselves for the WSRT data to pulses with $S/N > 16$, corresponding to $S/N > 1$ per channel, leaving 6755 main pulses and 650 interpulses. We use the AR data as a cross-check for possible systematics in the WSRT data, lowering the limit to $S/N > 10$ to have roughly the same sample of pulses, accounting for the ratio of 165/275 between the temperatures of the two telescope systems.

For each pulse pair, the correlation between their spectra gives $r(\Delta\nu)$ for a single value of Δt , the time separation of the pulses. We average these correlated spectra in equally spaced bins of Δt to construct our estimate of the correlation function. We show the result in Figure 3 for correlations between main-pulse pairs and for correlations between main-pulse and interpulse pairs (there are insufficient giant pulses associated with the interpulse to calculate a meaningful correlation function from those alone).

One sees that the correlations are fairly well defined and that the correlation of the main pulse with itself is clearly different from that with the interpulse, the latter being broader in both frequency and time, and having lower maximum correlation. More generally, one sees that the amplitudes of all correlations

are surprisingly low. We investigate the latter further in Section 4.1 but note here that it is not some systematic product of a given telescope: the results for WSRT and AR are entirely consistent with each other (as expected, as the giant pulses at both telescopes should differ only by noise and by systematics; space-ground VLBI results from Rudnistkii et al. (2017) measure a spatial scale of the scintillation pattern of $34,000 \pm 9000$ km during this observation, which is larger than the Earth’s radius).

For more quantitative measures, we fit the correlations with 2D Gaussians with variable amplitude, frequency, and time width. For the correlation between main pulse and interpulse, we additionally allow for offsets in time and frequency Δt_0 and $\Delta\nu_0$, where the sign convention used is IP–MP (e.g., a positive Δt_0 means the MP precedes the IP). For the main-pulse correlations, we find an amplitude of $1.80 \pm 0.03\%$ and decorrelation scales of $\nu_{\text{decorr}} = 1.10 \pm 0.02$ MHz in frequency, and $t_{\text{scint}} = 9.24 \pm 0.13$ s in time.¹⁰ The timescale is somewhat shorter than the value of 25 ± 5 s found at 1.475 GHz by Cordes et al. (2004), and the difference in observing frequency does not account for the difference (for $t_{\text{scint}} \propto \nu$, our measurement corresponds to 8.17 ± 0.12 s at 1.475 GHz). Differences are expected for observations at different epochs, however, as the scattering in the nebula is highly variable (Rankin & Counselman 1973; Lyne & Thorne 1975; Isaacman & Rankin 1977; Rudnistkii et al. 2017, and often showing “echoes,” e.g., Backer et al. 2000; Lyne et al. 2001; Driessen et al. 2019).

Our fits to the main-pulse to interpulse correlations confirm the qualitative impression from Figure 3 that compared to the main-pulse to main-pulse correlations, they are weaker and

¹⁰ We adopt the usual convention, defining ν_{decorr} and t_{scint} as the values where the correlation function drops to $1/2$ and $1/e$, respectively.

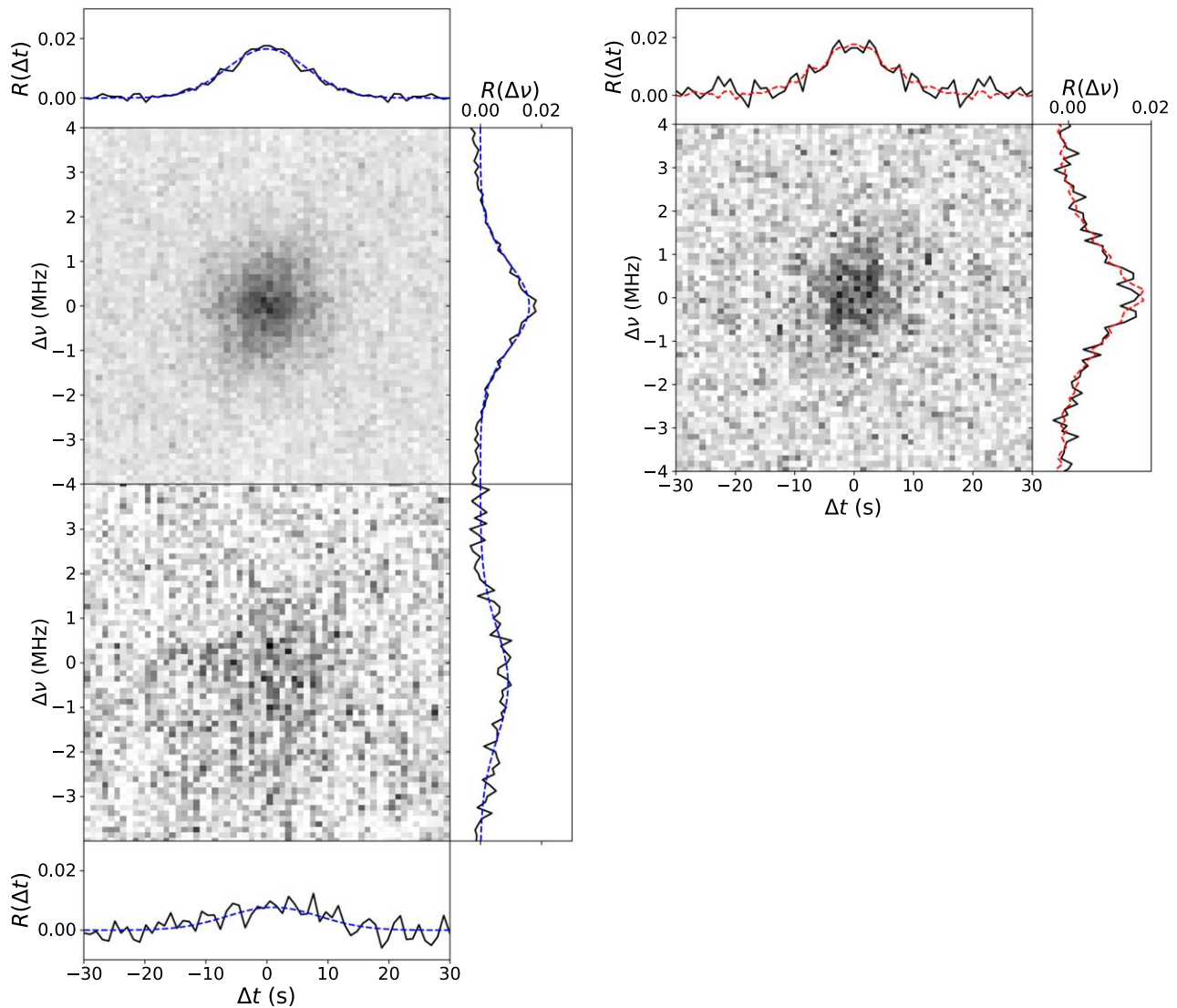


Figure 3. Left: Images: Cross-correlations $r(\Delta t, \Delta \nu)$ of pulse dynamic spectra between giant pulses in the main pulse with themselves (top) and with giant pulses in the interpulse (bottom). The correlation between main-pulse giant pulses is symmetric around the origin by construction (i.e., $r(\Delta t, \Delta \nu) = r(-\Delta t, -\Delta \nu)$), but this is not the case for the correlation between interpulse and main pulse. Side panels: a 10 bin (-5 – 5 s) and 9 bin (-0.5 – 0.5 MHz) wide average of correlations through the best-fit Δt , $\Delta \nu$, respectively. The dotted blue lines are the same cuts through the 2D Gaussian fits. Right: same as left, but using pulses at AR. The S/N is much lower owing to the higher T_{sys} value at AR (leading to fewer detected pulses, with lower S/N), and the shorter observation time. The dotted red line is the overlay of the MP–MP correlation at WSRT, showing that the two telescopes give consistent results.

broader in both frequency and time: the measured amplitude is $0.97 \pm 0.07\%$, $t_{\text{scint}} = 10.7 \pm 0.8$ s, and $\nu_{\text{decorr}} = 1.44 \pm 0.10$ MHz. We also find marginally significant time and frequency offsets of $\Delta t_0 = 1.02 \pm 0.54$ s and $\Delta \nu_0 = -0.34 \pm 0.09$ MHz.

To try to quantify the significance of these differences, we use simulated cross-correlations. Because we have many more giant pulses during the main pulse than the interpulse, we simply take 650 random main pulses (the number of inter-pulses above 16σ) for the cross-correlations and correlate them with the other 6755 main pulses, without correlating identical pulses. We repeat this 10,000 times and fit each subset with a 2D Gaussian, allowing for offsets in time and frequency Δt_0 and $\Delta \nu_0$. Comparing these with the value fit to the interpulse to main-pulse correlations (see Figure 4), the differences appear significant: none of the simulated data sets have as small an amplitude, or larger frequency offset $\Delta \nu_0$, while only relatively

small numbers have a larger time offset Δt_0 or wider frequency or time widths.

3.3. Comparison to Previous Work on the Same Data Set

The same data analyzed in this paper were studied in Rudnistkii et al. (2017) and Popov et al. (2017), who derive a decorrelation bandwidth of 279.2 ± 34.4 kHz, and 320 kHz, respectively. These values differ significantly from our value of $\nu_{\text{decorr}} = 1.10 \pm 0.02$ MHz, so here we further investigate the origin of these differences.

Our methods differ from those of Rudnistkii et al. (2017) and Popov et al. (2017); the crucial difference being that they autocorrelate individual giant pulses (between left and right circular polarization to reduce intrinsic structure correlating), while we correlate pulse pairs. For a direct comparison, we try to follow the steps of Popov et al. (2017), adopting their cutoff of SN > 22 , correlating left and right circular polarizations of

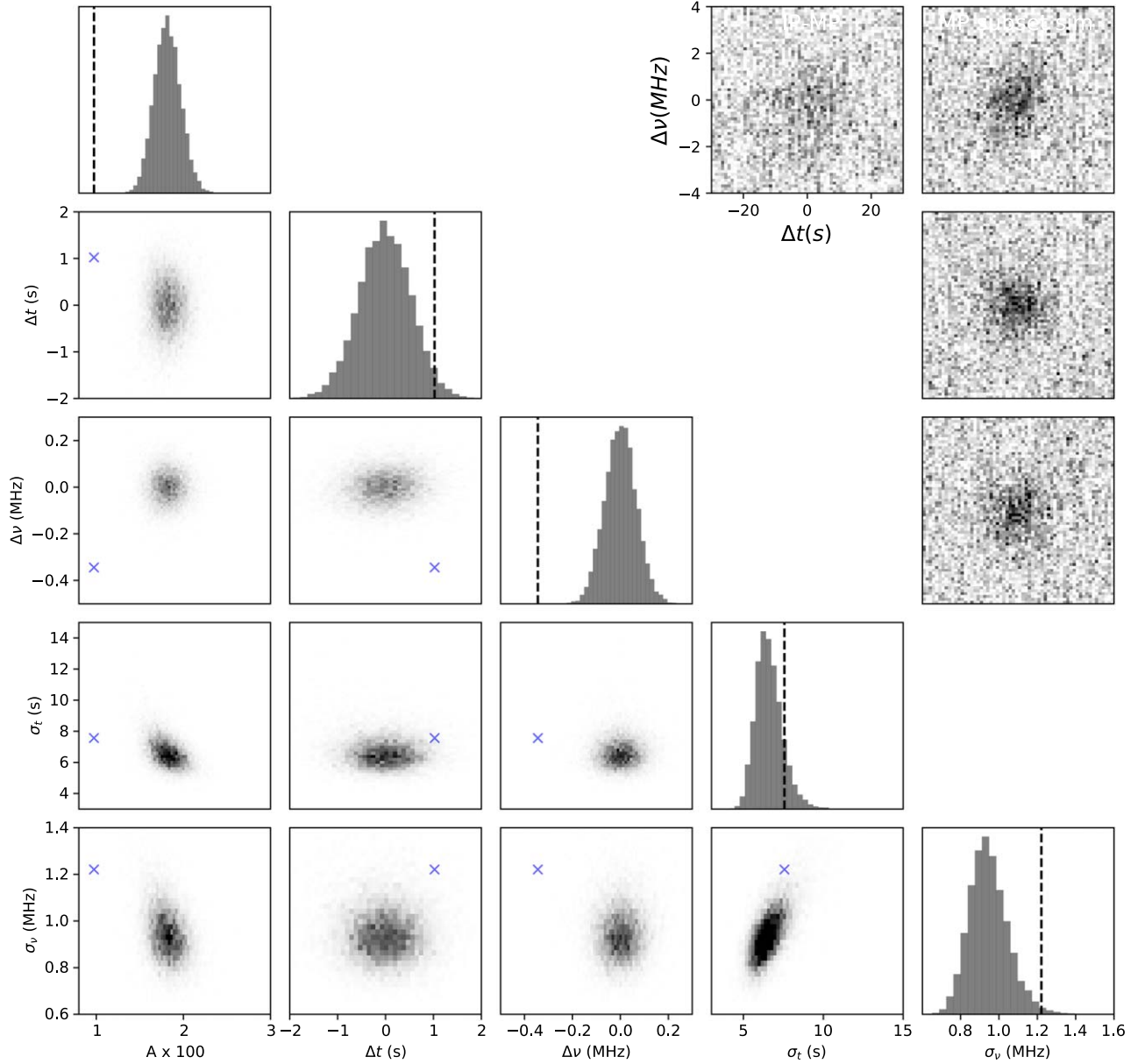


Figure 4. Bottom left: Corner plot of the best-fit parameters of the simulated interpulse to main-pulse correlation function obtained by fitting a two-dimensional Gaussian. Simulated correlation functions are constructed from randomly drawn sets of giant pulses from the main pulse (with the same sample size as that available for the interpulse), correlated with the full main-pulse sample. The dotted lines and the blue crosses show the best fit to the actual MP-IP correlation. Top right: The MP-IP correlation and three example simulated MP-IP plots for comparison.

each giant pulse and fitting a single exponential. From this, we measure $\nu_{\text{decorr}} = 0.39$ MHz, much closer to their value of $\nu_{\text{decorr}} = 0.32$ MHz. However, we find that a two-exponential fit is a much better fit to the data, giving two distinct scales of ν_{decorr} , $\nu_{\text{decorr}, 1} = 1.0$ MHz and $\nu_{\text{decorr}, 2} = 0.19$ MHz. This is consistent with our results if the small bandwidth ν_{decorr} is caused by intrinsic pulse structure (correlating only within the spectrum of a single pulse), and the wide bandwidth ν_{decorr} is the scintillation bandwidth (correlating between pulse pairs within t_{scint}).

Additionally, Rudnickii et al. (2017) derive a scintillation timescale of 22.4 ± 6.1 , which is larger than our value by a factor of 2. Their timescale is derived in a different way, where they use their measured scintillation bandwidth (described above), and angular size θ of the scattering screen, derived directly from their very long baseline interferometry (VLBI) correlation. Using the

known velocity of the Crab and an assumed isotropic scattering screen, we obtain a timescale estimate. Given the difference in our methods and the fact that the angular broadening likely arises in the interstellar medium rather than the nebula, the differences in these values are negligible.

3.4. Secondary Spectra

Pulsar scintillation is often best studied in terms of its conjugate variables τ and f_D , through their secondary spectrum $A(\tau, f_D) = \tilde{I}_1(\tau, f_D) \tilde{I}_2^*(\tau, f_D)$ (e.g., Stinebring et al. 2001; Briskin et al. 2010). The secondary spectrum is simply the Fourier transform of the correlation function $r(\Delta \nu, \Delta t) = I_1(\nu, t) \otimes I_2(\nu, t)$. For the MP-MP correlation, $A(\tau, f_D)$ is purely real, but in the MP-IP correlation, any time or frequency offsets in the correlation function will manifest as phase gradients in f_D or

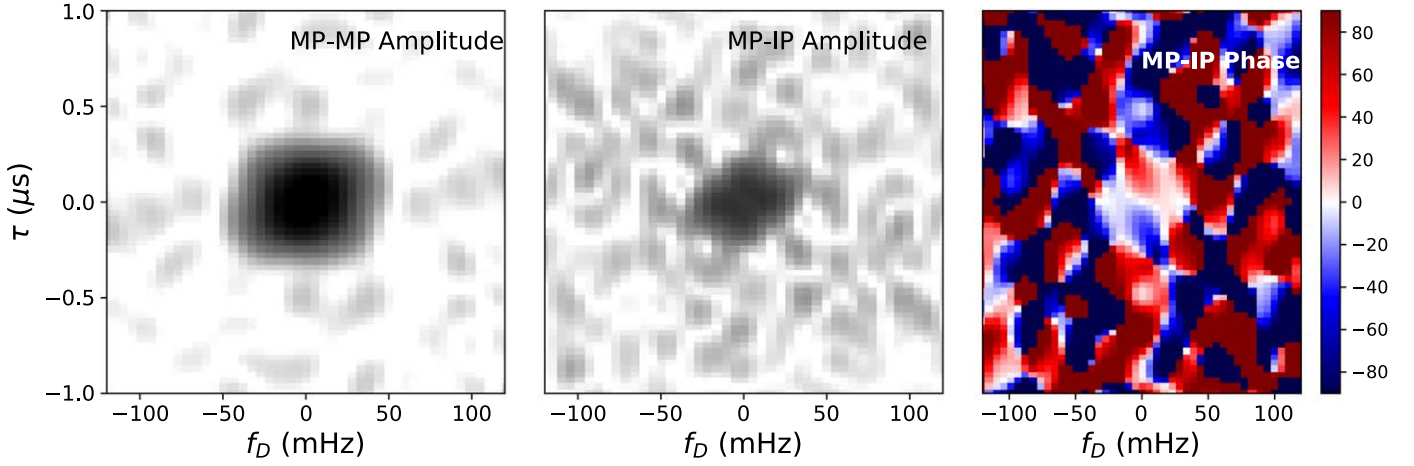


Figure 5. Left: Secondary spectrum of the main pulse. Middle and Right: Amplitude and phase of the main pulse—interpulse cross-spectrum. Note that the amplitude and phase are point-symmetric and point antisymmetric by definition. There appears to be a phase gradient in τ , reflecting the offset in frequency in the MP–IP correlation. Similarly, the possible phase gradient along f_D reflects the marginally significant offset in time between the main pulse and interpulse.

τ , respectively. We show the secondary spectra for both correlations after padding by 60 zero bins in time in Figure 5.

The MP–IP secondary spectrum is dominated by a phase gradient in τ , arising from the frequency offset in the correlation function. Removing a linear phase gradient in τ shows a marginally significant phase gradient in f_D . If the screen were 1D and the main pulse and interpulse emission locations were offset, there would be a phase gradient in f_D , independent of τ .

4. Ramifications

4.1. The Surprisingly Low Correlation Coefficient

Giant pulses are on average a few μs in duration and are comprised of many smaller, unresolved “nanoshots” (e.g., Hankins & Eilek 2007). However, if all nanoshots originate from the same projected physical location, they should all be imparted with the same impulse response function; an identical signal would correlate perfectly, and a signal with many random polarized shots with the same impulse response should correlate no worse than one-third (Cordes et al. 2004, Appendix).

The observed $\sim 2\%$ correlation between main pulses is well below the expectation of one-third. This could be explained if individual pulses come from small parts of the full extended emission region, which is larger than the resolution of the scattering screen (discussed in the following section). Following this explanation, the correlation should decrease even further during times of higher nebular scattering—we investigate this further in R. Lin et al. (2021, in preparation).

4.2. Spatial Resolution of the Scattering Screen

The size and location of the scattering screen is not precisely known, but a model in which the majority of the temporal scattering occurs in the Crab Nebula is favored by VLBI measurements showing that the visibility amplitude is constant through the scattering tail, and independent of the scattering time (Vandenberg et al. 1976; Vandenberg 1976) as well as by the short scintillation timescale (Cordes et al. 2004).

Because scattering requires relatively large differences in (electron) density, it is very unlikely to occur inside the pulsar-wind filled interior of the Crab Nebula, which must have very low density. For a reasonable bulk magnetic field of 10^{-4} G,

the emitting radio electrons are very relativistic, with $\gamma \sim 10^3$. The radio-emitting electrons have a density of $n_e \approx 10^{-5} \text{ cm}^{-3}$ (Shklovsky 1957), implying that the refractive index deviates from unity by a tiny amount,

$$\Delta n \approx \left(\frac{\nu_p}{\nu} \right)^2 \sim 10^{-18}, \quad (3)$$

where $\nu_p = (e^2 n_e / \pi \gamma m_e)^{1/2}$ is the plasma frequency, and ν is the observed radio frequency.

Instead, the only plausible location for the temporal scattering is in the optically emitting filaments in the Crab Nebula, which have $n_e \sim 1000 \text{ cm}^{-3}$ (Osterbrock 1957). These filaments develop because as the pulsar wind pushes on the shell material, the contact discontinuity accelerates, leading to the RT instability (Chevalier 1977; Porth et al. 2014).

With 3D models fit to optical spectroscopic data of the Crab Nebula, Lawrence et al. (1995) find that the filaments reside conservatively in the range $\sim 0.5\text{--}2.0$ pc when a nominal pulsar distance of 2 kpc is used.

The scattering causes a geometric time delay given by

$$\tau = \frac{\theta^2 d_{\text{eff}}}{2c}, \quad \text{with} \quad d_{\text{eff}} = \frac{d_{\text{psr}} d_{\text{lens}}}{d_{\text{psr}} - d_{\text{lens}}}, \quad (4)$$

where θ is the angle the screen extends to as seen from Earth, and d_{psr} and d_{lens} are the distances to the pulsar and the screen, respectively.

The scattering screen can be seen as a lens, with physical size $D = \theta d_{\text{lens}}$ and corresponding angular resolution λ/D , giving a physical resolution at the pulsar of $\Delta x = (d_{\text{psr}} - d_{\text{lens}}) \lambda / \theta d_{\text{lens}}$, or, in terms of the scattering time τ ,

$$\Delta x = \frac{\lambda}{\sqrt{2}\pi} \left(\frac{d_{\text{psr}} - d_{\text{lens}}}{2c\tau} \frac{d_{\text{psr}}}{d_{\text{lens}}} \right)^{1/2}. \quad (5)$$

The prefactor $1/\sqrt{2}\pi$ is model dependent, coming from using a square-law ($\alpha = 2$) phase-structure function (Cordes & Rickett 1998).

If we were to infer the scattering time from the scintillation bandwidth, we would find $\tau_{\text{scint}} = 1/2\pi\Delta\nu \simeq 160$ ns, using $\Delta\nu \simeq 1$ MHz. However, this is lower than the apparent $\sim 1 \mu\text{s}$ scattering seen in Figure 1 and lower than measurements of the

scattering at this epoch of $\tau(600 \text{ MHz}) \simeq 0.1 \text{ ms}$ (McKee et al. 2018), or $\tau(350 \text{ MHz}) \simeq 0.6 \text{ ms}$ (Driessen et al. 2019), which would correspond to $\tau \simeq 1.1\text{--}1.7 \mu\text{s}$ when scaled by $\tau \propto \nu^{-4}$ to our observing frequency. In Gwinn et al. (1998), it is noted that the relation $\tau = 1/2\pi\Delta\nu$ may underestimate τ in the case of an extended, resolved emission region as

$$\tau = \frac{\sqrt{1 + 4\sigma_1^2}}{2\pi\Delta\nu}, \quad (6)$$

where σ_1 is the size of the emission region in units of the lens resolution. In this picture, the scintillation timescale would depend on the lens resolution and the emission region size.

Using $\tau \simeq 1 \mu\text{s}$ and $d_{\text{psr}} - d_{\text{lens}} \simeq 1.0 \text{ pc}$, then $\Delta x \simeq 290 \text{ km}$ (for the full range of allowed distances, $205 \lesssim \Delta x \lesssim 410 \text{ km}$). Thus, the resolution of the scattering screen is smaller than the light-cylinder radius of the Crab pulsar, $R_{\text{LC}} \equiv cP/2\pi = 1600 \text{ km}$.

Additionally, a nominal time offset between the main pulse and interpulse of $\sim 1\text{--}2 \text{ s}$ is $\sim 10\%\text{--}20\%$ of the scintillation timescale, which would suggest that the emission locations are separated by hundreds of kilometers. We could turn a measured time offset into a physical separation given the relative velocity between the pulsar and the screen. Unfortunately, this is not known, although we can set limits from the proper motion. The proper motion of the Crab pulsar relative to its local standard of rest is measured to be $12.5 \pm 2.0 \text{ mas yr}^{-1}$ in the direction $290^\circ \pm 9^\circ$ (east of north; Kaplan et al. 2008), where the uncertainties attempt to account for the uncertainty in the velocity of its progenitor, and therewith, of the nebular material. At an assumed distance of 2 kpc , the implied relative velocity of the pulsar is $\sim 120 \text{ km s}^{-1}$, and nonradial motions in the filaments can be up to $\sim 70 \text{ km s}^{-1}$ (Backer et al. 2000). A $1\text{--}2 \text{ s}$ time delay between pulse components would then suggest a projected separation between the interpulse and main-pulse emission regions of $\sim 50\text{--}400 \text{ km}$.

As mentioned above, Cordes et al. (2004) argue that the short scintillation timescale suggests a nebular origin of the observed scintillation. Here we outline the argument using our measured values. The scintillation timescale is roughly the time it takes for the extended emission region to traverse a resolution element of the scattering screen; using the above resolution and proper motion gives an estimate of the timescale of $\sqrt{\sigma_1^2 + 1} \Delta x / v_{\text{pm}} \sim 5.5\text{--}11 \text{ s}$, consistent with our observed time of $9.24 \pm 0.13 \text{ s}$.

Scintillation in the interstellar screen for our given scintillation bandwidth would result in much higher resolution elements (for a screen halfway to the pulsar, at $d_{\text{psr}} - d_{\text{lens}} \simeq 1 \text{ kpc}$, greater by a factor $\sim \sqrt{1 \text{ kpc}/1 \text{ pc}} \sim 30$) and scintillation on several-minute timescales, which is more typical of interstellar scintillation in this frequency range.

If we assume that pulses occur at a random position within an extended region, we may also estimate the average expected correlation. To test this, we simulated 500 pulses with positions drawn at random from a 2D Gaussian with $\sigma_{xy} = \sigma_1 \Delta x$. The correlation coefficient between each pair of pulses is estimated as $r_{ij} = C e^{-|x_{ij}|^2/(\Delta x)}$, where $|x_{ij}|$ is the projected position difference between each pulse pair, and $C < 1$ is an unknown constant that depends on both the intrinsic spectral structure in the pulses (e.g., Cordes et al. 2004 and the Appendix) and on whether the separate components forming giant pulses are resolved. Assuming an isotropic 2D screen or a 1D screen,

and assuming $C = 1/3$ (i.e., that individual giant pulses are unresolved, which may not be a good assumption), gives estimates of the expected correlation coefficient of $\langle r_{1D} \rangle \simeq 0.071$, $\langle r_{2D} \rangle \simeq 0.016$, respectively, which is on the same order as our observed average correlation coefficient. We find that the assumed picture of giant pulses occurring in an extended region of $\sim 1000 \text{ km}$ gives a consistent result that broadly agrees with the observed scintillation bandwidth, scintillation timescale, and low correlation coefficient. This picture will be expanded in more detail in R. Lin et al. (2021, in preparation).

The picture we find above differs from that reported by Cordes et al. (2004), who find that the spectra of nearby pulses at 1.48 GHz and 2.33 GHz correlate at a value of $\sim 1/3$. They find values of the scintillation bandwidth and timescale at 2.33 GHz of $\Delta\nu_s = 2.3 \pm 0.4 \text{ MHz}$ and $\Delta t_s = 35 \pm 5 \text{ s}$, which, scaled to 1.68 GHz , gives $\Delta\nu = 0.6 \pm 0.1 \text{ MHz}$, and $\Delta t = 25 \pm 4 \text{ s}$ (Cordes et al. 2004 also consistently find $\Delta\nu_s < 0.8 \text{ MHz}$, $\Delta t_s = 25 \pm 5 \text{ s}$ at 1.48 GHz). They face a similar inconsistency between the measured scattering time ($\sim 0.1 \text{ ms}$ at 600 MHz , which implies $\sim 1.7 \mu\text{s}$ at 1 . McKee et al. 2018) and the inferred scattering time from $1/2\pi\Delta\nu \approx 250 \text{ ns}$. However, the scintillation time they measure is much longer than ours, implying that the dominant screen must be at a greater distance from the pulsar or be anisotropic and oriented such that there is poorer resolution along the direction of the relative velocity between the pulsar and the screen.

4.3. Fully Quantifying Emission Sizes and Separations

A major uncertainty in our above estimates is the geometry of the lens. From studies of the scintillation in other pulsars, the scattering screens in the interstellar medium are known to be highly anisotropic, as demonstrated most dramatically by the VLBI observations of Brisken et al. (2010). If the same holds for the nebular scattering screens, this implies that our resolution elements are similarly anisotropic. Because the orientation relative to the proper motion is unknown, the physical distance between the main and interpulse regions could be either smaller or larger than our estimate above. Because the scattering varies with time, it may be possible to average these effects out.

With a perfectly 1D scattering screen, it is difficult to produce both a time and frequency offset as there would necessarily be some position where the main pulse and interpulse pass through the same position along the screen axis. One possible way to induce a frequency offset would be a spatial gradient of the column density (or ‘‘prism’’) on the scale of the separation between emission regions. Our frequency offset of $\sim 0.3 \text{ MHz}$ could be explained by a DM gradient of $\Delta\text{DM}/\text{DM} \sim 0.02\%$ over $\sim 1000 \text{ km}$. The DM variations of the Crab have not been probed on these small spatial scales, although it varies by considerably more than this on longer timescales (i.e., larger spatial scales, e.g., McKee et al. 2018). For two spatially separated emission components, Ravi & Deshpande (2018) find that a 2D screen can produce both a time and frequency shift over a short timescale. The two-dimensionality of the screen, or the effect of multiple scattering screens, may need to be considered.

Furthermore, all values relating to the scattering screen include the uncertain distance to the Crab pulsar, suggesting that a parallax distance would improve our constraints. In addition, the rough localization of the scattering in the

filaments is based on physical arguments; the results would be greatly improved through a direct measurement.

The distance to the screen(s) can be constrained through VLBI and through scintillation measurements across frequency. As the spatial broadening of the Crab is dominated by the interstellar screen rather than the nebula, VLBI at space-ground baselines (Rudnitskii et al. 2016) or at low frequencies (Vandenberg 1976) can help constrain the angular size of the scattering in the interstellar medium. This in turn can constrain the size of the nebular screen. The visibility amplitudes will only decrease below 1 when the scattered image of the pulsar is not point-like to the interstellar screen. Time-resolved visibilities throughout the rise time of scattered pulses may then elucidate the nebular scale; by increasing in time delay, one increases in angular size and thus resolution, so one may observe the transition point beyond which the nebular screen becomes resolved. In addition, the interstellar screen will scintillate only when it does not resolve the nebular screen (the same argument has been made for scintillation in fast radio bursts; Masui et al. 2015). The transition frequency for the two scintillation bandwidths to become apparent in the spectra could give a size measurement of the nebular screen.

Applying this same analysis across different frequencies or in times of different scattering in the nebula will also help to quantify both the separation of the main pulse and interpulse, and the size of the emitting regions of both components. The correlation function of spectra is a crude measurement—it is fourth order in the electric field, and the scintillation pattern is contaminated with intrinsic pulse substructure. A much cleaner measurement can hopefully be made in the regime where the duration of giant pulses is much shorter than the scattering time, akin to the coherent method of descattering pulses in Main et al. (2017).

As discussed in Section 4.2, we associate the scattering screen with the filaments in the pulsar wind nebula (Porth et al. 2014). These filaments appear from the Rayleigh–Taylor instability, when the pulsar wind pushes and accelerates freely expanding envelope. This stage terminates after few thousand years when the reverse shock from the interaction between the supernova remnant at the interstellar medium reaches the pulsar wind nebula (Gelfand et al. 2009, see review by Slane 2017). Thus we expect these special scattering environments to be specific for pulsar wind nebulae during a fairly short period—sufficiently young for the reverse shock not to reach the pulsar wind nebula, but sufficiently advanced to have Rayleigh–Taylor-induced filaments.

We thank the anonymous referee, whose comments greatly improved the draft. We thank Judy Xu, who attempted the initial 1D correlation function of giant pulses. These data were taken as part of a RadioAstron observing campaign. The RadioAstron project is led by the Astro Space Center of the Lebedev Physical Institute of the Russian Academy of Sciences and the Lavochkin Scientific and Production Association under a contract with the State Space Corporation ROSCOSMOS, in collaboration with partner organizations in Russia and other countries.

Appendix

Correcting Noise Biases in the Correlation Coefficient

The intrinsic correlation coefficient between two pulse spectra $P_{1,2}(\nu)$ can be generally defined as

$$\rho(P_1, P_2) = \frac{\langle (P_1(\nu) - \mu_1)(P_2(\nu) - \mu_2) \rangle}{\sigma_1 \sigma_2}, \quad (\text{A1})$$

where $\langle \dots \rangle$ indicates the expectation value for an average over frequency, and μ and σ^2 are expectation values of the mean and variance, respectively. With this definition, one will have $\rho = 1$ for two pulses with identical frequency structure.

Typically, as an estimate of ρ , one uses the sample correlation coefficient,

$$r(P_1, P_2) = \frac{1}{k-1} \times \sum_{i=1}^k \frac{(P_1(\nu_i) - m_1)(P_2(\nu_i) - m_2)}{s_1 s_2}, \quad (\text{A2})$$

where k is the number of frequency bins, and m_p and s_p^2 are the usual sample mean and variance. In the presence of noise, subtracting m leaves the nominator unbiased, but s^2 will be systematically higher than σ^2 , and thus r will be biased low. For normally distributed data, one could approximately correct with $s_{\text{int}}^2 = s_p^2 - s_n^2$, but this does not hold for our case of power spectra.

Here, we derive an expression that is valid for our case, where we wish to ensure that $\langle r \rangle = 1$ for two pulses that are sufficiently short for us to approximate them as delta functions and that are affected by the interstellar medium in the same way, i.e., have the same impulse response function $g(t)$. In this case, the measured electric field of a giant pulse is

$$E_p(\nu) = A_p g(\nu) + n(\nu), \quad (\text{A3})$$

where A_p is the amplitude of the pulse's delta function in the Fourier domain, and $g(\nu)$ and $n(\nu)$ are the Fourier transforms of the impulse response function and the measurement noise, respectively. The measured intensity is then

$$P_p(\nu) = E_p^2(\nu) = A_p^2 g^2(\nu) + n^2(\nu) + 2A_p |g(\nu)| |n(\nu)| \cos(\Delta\phi(\nu)), \quad (\text{A4})$$

where $\Delta\phi(\nu)$ is the phase difference between $n(\nu)$ and $g(\nu)$, and where squares are of the absolute values.

The expectation value for the average is

$$\mu_p = \langle P_p \rangle = A_p^2 \langle g^2 \rangle + \langle n^2 \rangle, \quad (\text{A5})$$

where we have dropped the dependencies on frequency for brevity, and used that the cross term averages to zero because $\langle \cos(\Delta\phi) \rangle = 0$. Hence, the expectation value for the variance is

$$\sigma_p^2 = A_p^4 [\langle g^4 \rangle - \langle g^2 \rangle^2] + \langle n^4 \rangle - \langle n^2 \rangle^2 + 4A_p^2 \langle g^2 n^2 \cos^2(\Delta\phi) \rangle, \quad (\text{A6})$$

where we have again omitted terms that average to zero. The last term does not average to zero because of the squaring: it reduces to $2A_p^2 \langle g^2 \rangle \langle n^2 \rangle$ because g and n are independent and $\langle \cos^2(\Delta\phi) \rangle = 1/2$.

For two pulses differing only by noise, the expectation value for the numerator of r is

$$\begin{aligned} & \langle (P_1(\nu) - \mu_1)(P_2(\nu) - \mu_2) \rangle \\ &= A_1^2 A_2^2 [\langle g^4 \rangle - \langle g^2 \rangle^2]. \end{aligned} \quad (\text{A7})$$

Thus, for an unbiased estimate of r , we need to estimate $\sigma_p = A_p^2 [\langle g^4 \rangle - \langle g^2 \rangle^2]^{1/2}$. We can do this by also measuring the properties of the background, which if dominated by

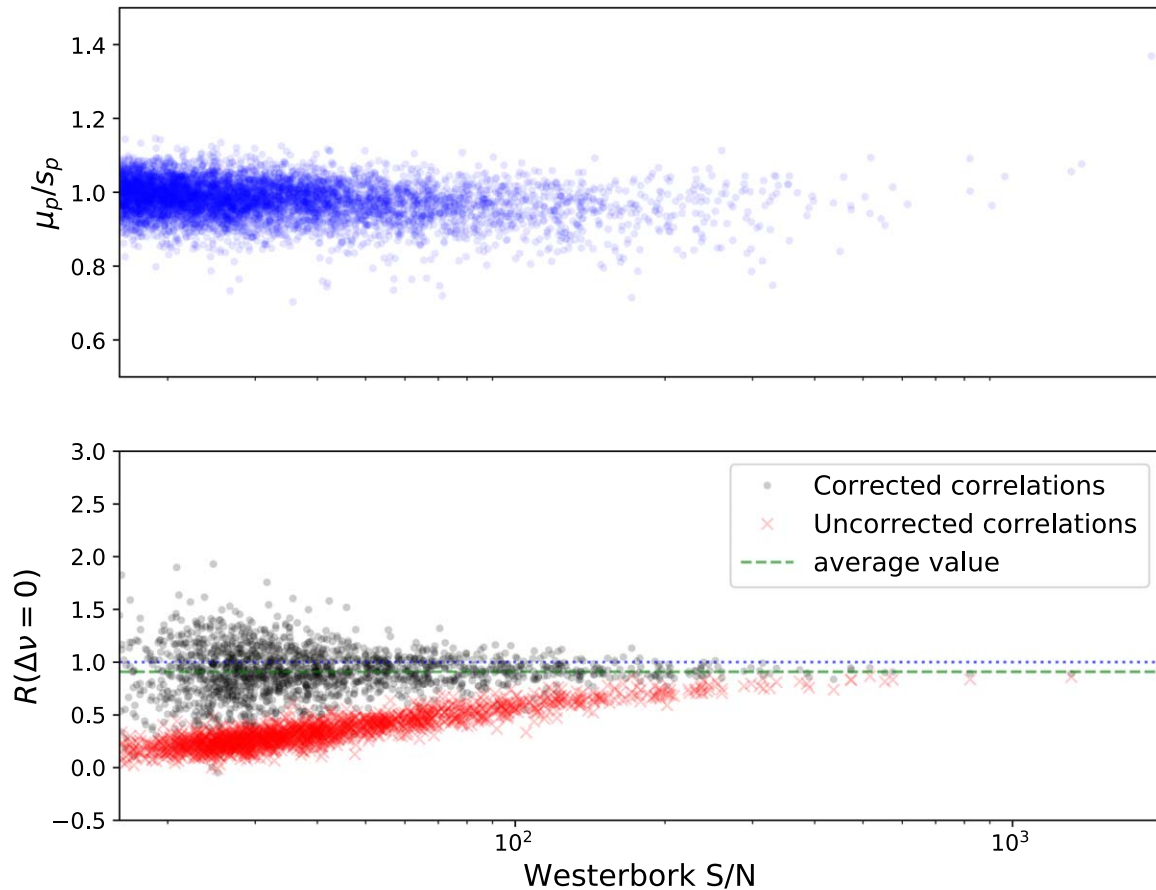


Figure A1. Top: Ratio of the mean and standard deviation of every giant pulse spectrum. It averages at 1 independently of S/N, showing that it is reasonable to use this as an assumption to correct for our correlation coefficients. Bottom: Sample correlation coefficients of giant pulse spectra for each pulse detected above 16σ at both WSRT and AR, ordered by increasing S/N. For the black points, the noise correction described in the Appendix has been applied, while no correction has been applied for the red points (i.e., the standard formula for the sample correlation coefficient has been used).

measurement noise with the same properties as the pulse, has $\mu_b = \langle n^2 \rangle$ and $s_b^2 = \langle n^4 \rangle - \langle n^2 \rangle^2$ (this will underestimate the noise if the pulse is strong enough to raise the system temperature, although in this case, the noise has only a small contribution to the variance of the pulse and is negligible in computing r). With this, it follows that to make estimates of r free of noise bias, we should use

$$s_{\text{int}}^2 = s_p^2 - s_b^2 - 2(\mu_p - \mu_b)\mu_b. \quad (\text{A8})$$

This is a noisy quantity, however, and simply replacing the measured variance with this value will lead to some measured values of $s_{\text{int}} \sim 0$, and thus diverging correlations.

Instead of correcting the sample variances in the denominator of the sample correlation coefficient, one can use the properties of the pulse to estimate a correction of the sample correlation coefficient itself. Assuming the impulse response function $g(\nu)$ is approximately normally distributed, the power spectrum $|g(\nu)|^2$ will be distributed roughly as a χ^2 distribution with two degrees of freedom, with $s_p^2 \simeq m_p^2$. Using this, our unbiased estimate of the variance simplifies to $s_{\text{int}}^2 = (m_p - m_b)^2$, which uses the well-measured mean of both the pulse and the background (in our case, after the bandpass calibration described in Section 2, the mean and standard deviation of the background are unity).

We should not use the above estimate directly in the denominator of the standard correlation coefficient in

Equation (A1) because at high S/N, this unnecessarily introduces additional variance. Instead, we can ensure an unbiased, noise-corrected estimate of the correlation that works at both low and high S/N by writing it as

$$r(P_1(\nu), P_2(\nu)) = \frac{\langle (P_1(\nu) - m_1)(P_2(\nu) - m_2) \rangle}{s_1 s_2} \times \left(\frac{m_1 m_2}{(m_1 - m_b)(m_2 - m_b)} \right). \quad (\text{A9})$$

To test our correlation correction, we first verify our underlying assumption that the mean and standard deviation are equal by taking the ratio of the measured values for all pulses. The result is shown in the top panel of Figure A1: one sees that the ratio is around unity, except at the highest S/N, where saturation biases the noise low. Next, we correlated the spectra of all overlapping pulses between WSRT and AR with S/N > 16 at both telescopes, shown in the bottom panel of Figure A1. Because these are the same pulses, but observed at two different telescopes and thus with different noise, we expect values to scatter around unity. Indeed, using the full noise correction, we find that the sample correlations are around a value close to unity, of $\sim 90\%$, independently of S/N (the difference from 100% likely reflects remaining differences in bandpass etc.; the baseline is too short for interstellar scintillation to differ). Without the correction, the sample correlation coefficient is always lower than 100% and decreases with decreasing S/N.

For a further test, we use simulated giant pulses. To begin, pulses are simulated as identical delta function giant pulses with the same impulse response function, but different noise, in the manner described in Main et al. (2017). We find that using the above estimates, the correlation coefficients between these pulses indeed average to unity. Trying a slightly more realistic simulation, forming giant pulses with N fully polarized shots, with random amplitudes (drawn from a normal distribution) and random phases, the correlation decreases, saturating at $r=1/3$ for large numbers ($N \gtrsim 10$), in line with what is expected from the derivation in Cordes et al. (2004).

Finally, all of the above is for correlations of the power spectra of a single polarization, and throughout the paper, we correlate each polarization separately, then average the two values. For completeness, we note that if one were to use the total intensity $I = P_L + P_R = P_X + P_Y$, under the assumption that the noise is not correlated between the polarizations, the expectation value for the standard deviation is

$$\sigma_I^2 = A_p^4 [\langle g^4 \rangle - \langle g^2 \rangle^2] + \langle n^4 \rangle - \langle n^2 \rangle^2 + 2A_p^2 \langle g^2 n^2 \cos^2(\Delta\phi) \rangle, \quad (\text{A10})$$

and a noise-corrected estimate can be made with

$$s_{\text{int}}^2 = s_I^2 - s_b^2 - (\mu_I - \mu_b)\mu_b, \quad (\text{A11})$$

with the cross term differing by a factor of 2 from the single-polarization case. Adding more samples with independent noise, the cross term further diminishes and can be treated as Gaussian in the limit of large N . We do not use these estimates, however, because when the giant pulses are not single delta functions, the estimates start to depend on the degree of polarization (Cordes et al. 2004), which is a complication we would rather avoid.

ORCID iDs

Robert Main  <https://orcid.org/0000-0002-7164-9507>
 Marten H. van Kerkwijk  <https://orcid.org/0000-0002-5830-8505>
 Ue-Li Pen  <https://orcid.org/0000-0003-2155-9578>
 Alexei G. Rudnitskii  <https://orcid.org/0000-0003-1798-9444>
 Maxim Lyutikov  <https://orcid.org/0000-0001-6436-8304>

References

Abdo, A. A., Ackermann, M., Ajello, M., et al. 2010, *ApJ*, 708, 1254
 Backer, D. C., Wong, T., & Valanju, J. 2000, *ApJ*, 543, 740
 Brisken, W. F., Macquart, J.-P., Gao, J. J., et al. 2010, *ApJ*, 708, 232
 Chevalier, R. A. 1977, *ARA&A*, 15, 175

Cordes, J. M., Bhat, N. D. R., Hankins, T. H., McLaughlin, M. A., & Kern, J. 2004, *ApJ*, 612, 375
 Cordes, J. M., & Rickett, B. J. 1998, *ApJ*, 507, 846
 Driessen, L. N., Janssen, G. H., Bassa, C. G., Stappers, B. W., & Stinebring, D. R. 2019, *MNRAS*, 483, 1224
 Eilek, J. A., & Hankins, T. H. 2016, *JPIPh*, 82, 635820302
 Enoto, T., Terasawa, T., Kisaka, S., et al. 2021, *Sci*, 372, 187
 Gelfand, J. D., Slane, P. O., & Zhang, W. 2009, *ApJ*, 703, 2051
 Gupta, Y., Bhat, N. D. R., & Rao, A. P. 1999, *ApJ*, 520, 173
 Gwinn, C. R., Britton, M. C., Reynolds, J. E., et al. 1998, *ApJ*, 505, 928
 Hankins, T. H., & Eilek, J. A. 2007, *ApJ*, 670, 693
 Hankins, T. H., Eilek, J. A., & Jones, G. 2016, *ApJ*, 833, 47
 Isaacman, R., & Rankin, J. M. 1977, *ApJ*, 214, 214
 Istomin, Y. N. 2004, in IAU Symp. 218, Young Neutron Stars and Their Environments, ed. F. Camilo & B. M. Gaensler (San Francisco, CA: ASP), 369
 Jenet, F. A., & Anderson, S. B. 1998, *PASP*, 110, 1467
 Kaplan, D. L., Chatterjee, S., Gaensler, B. M., & Anderson, J. 2008, *ApJ*, 677, 1201
 Karuppusamy, R., Stappers, B. W., & van Straten, W. 2010, *A&A*, 515, A36
 Lawrence, S. S., MacAlpine, G. M., Uomoto, A., et al. 1995, *AJ*, 109, 2635
 Lyne, A. G., Pritchard, R. S., & Graham-Smith, F. 1993, *MNRAS*, 265, 1003
 Lyne, A. G., Pritchard, R. S., & Graham-Smith, F. 2001, *MNRAS*, 321, 67
 Lyne, A. G., & Thorne, D. J. 1975, *MNRAS*, 172, 97
 Main, R., van Kerkwijk, M., Pen, U.-L., Mahajan, N., & Vanderlinde, K. 2017, *ApJL*, 840, L15
 Masui, K., Lin, H.-H., Sievers, J., et al. 2015, *Natur*, 528, 523
 McKee, J. W., Lyne, A. G., Stappers, B. W., Bassa, C. G., & Jordan, C. A. 2018, *MNRAS*, 479, 4216
 Moffett, D. A., & Hankins, T. H. 1996, *ApJ*, 468, 779
 Muslimov, A. G., & Harding, A. K. 2004, *ApJ*, 606, 1143
 Osterbrock, D. E. 1957, *PASP*, 69, 227
 Pen, U.-L., Macquart, J.-P., Deller, A. T., & Brisken, W. 2014, *MNRAS*, 440, L36
 Petrova, S. A. 2004, *A&A*, 424, 227
 Petrova, S. A. 2009, *MNRAS*, 395, 1732
 Philippov, A., Uzdensky, D. A., Spitkovsky, A., & Cerutti, B. 2019, *ApJL*, 876, L6
 Popov, M. V., Rudnitskii, A. G., & Soglasnov, V. A. 2017, *ARep*, 61, 178
 Porth, O., Komisarov, S. S., & Keppens, R. 2014, *MNRAS*, 443, 547
 Qiao, G. J., Lee, K. J., Wang, H. G., Xu, R. X., & Han, J. L. 2004, *ApJL*, 606, L49
 Rankin, J. M., & Counselman, C. C., III 1973, *ApJ*, 181, 875
 Ravi, K., & Deshpande, A. A. 2018, *ApJ*, 859, 22
 Romani, R. W., & Yadigaroglu, I.-A. 1995, *ApJ*, 438, 314
 Rudnitskii, A. G., Popov, M. V., & Soglasnov, V. A. 2017, *ARep*, 61, 393
 Rudnitskii, A. G., Karuppusamy, R., Popov, M. V., & Soglasnov, V. A. 2016, *ARep*, 60, 211
 Shearer, A., Stappers, B., O'Connor, P., et al. 2003, *Sci*, 301, 493
 Shklovsky, I. S. 1957, in IAU Symp. 4, Radio Astronomy, ed. H. C. van de Hulst (Cambridge: Cambridge Univ. Press), 201
 Slane, P. 2017, Pulsar Wind Nebulae (Berlin: Springer International), 2159
 Smirnova, T. V., Shishov, V. I., & Malofeev, V. M. 1996, *ApJ*, 462, 289
 Stinebring, D. R., McLaughlin, M. A., Cordes, J. M., et al. 2001, *ApJL*, 549, L97
 Strader, M. J., Johnson, M. D., Mazin, B. A., et al. 2013, *ApJL*, 779, L12
 Vandenberg, N. R. 1976, *ApJ*, 209, 578
 Vandenberg, N. R., Clark, T. A., Erickson, W. C., Resch, G. M., & Broderick, J. J. 1976, *ApJ*, 207, 937
 Wolszczan, A., & Cordes, J. M. 1987, *ApJL*, 320, L35